THE ASTRONOMICAL JOURNAL VOLUME 112, NUMBER 1 JULY 1996

INFRARED SPECTROSCOPY OF Paβ AND [Fe II] EMISSION IN NGC 4151

R. A. KNOP, L. ARMUS, J. E. LARKIN,[1] K. MATTHEWS, D. L. SHUPE,[2], AND B. T. SOIFER
Palomar Observatory, The California Institute of Technology, Pasadena, California 91125
Electronic mail: rknop@mop.caltech.edu

Received 1995 December 7; revised 1996 March 27

NASA-CR-205258

ABSTRACT

We present spatially resolved 1.24–1.30 μm spectroscopy with a resolution of 240 km/s of the Seyfert 1.5 galaxy NGC 4151. Broad Paβ, narrow Paβ, and narrow [Fe II] ($\lambda=1.2567$ μm) emission lines are identified in the spectrum. Additionally, a spatially unresolved narrow component probably due to [S IX] ($\lambda=1.25235$ μm) is observed on the nucleus. The narrow Paβ and [Fe II] lines are observed to be extended over a scale of 5″. The spatial variation of the velocity centers of the Paβ and [Fe II] lines show remarkable similarity, and additionally show similarities to the velocity structure previously observed in ground based spectroscopy of [O III] emission in NGC 4151. This leads to the conclusion that the [Fe II] emission arises in clouds in the Seyfert narrow line region that are physically correlated with those narrow line clouds responsible for the optical emission. The [Fe II] emission line, however, is significantly wider than the Paβ emission line along the full spatial extent of the observed emission. This result suggests that despite the correlation between the bulk kinematics of Paβ and [Fe II], there is an additional process, perhaps fast shocks from a wind in the Seyfert nucleus, contributing to the [Fe II] emission. © *1996 American Astronomical Society.*

1. INTRODUCTION

Nearby Seyfert galaxies provide a laboratory for studying the properties of the nuclear and near-nuclear emission surrounding an Active Galactic Nucleus (AGN) with the best possible spatial resolution. One of the goals of studies of nearby Seyfert galaxies is to understand the dynamics, excitation mechanisms, and ionization structure of the circumnuclear gas. Infrared spectroscopy complements optical spectral studies of the nuclear regions of these systems in that infrared radiation is less affected by dust extinction, and in that recombination lines, low ionization collisionally excited atomic transitions, as well as lines from warm molecular gas, are strong in the *J*, *H*, and *K* band atmospheric windows. The study of the correspondence between infrared and optical spectral characteristics of Seyfert galaxies should produce a more complete picture of the physical environment of these systems, including the interactions of the ionized gas with the surrounding molecular material.

The nearby galaxy NGC 4151, being one of the brightest and best studied Seyfert galaxies, is an ideal candidate for these spatially resolved infrared spectral studies. NGC 4151 has been classified optically as a Seyfert 1.5 galaxy (Osterbrock & Koski 1975). From measurements of the 21 cm H I line in the outer parts of the galactic disk, Pedlar *et al.* (1992) derive a systemic radial velocity of 997±3 km/s. Using a value of 75 km s^{-1} Mpc^{-1} for H_0 yields a distance to NGC 4151 of 13 Mpc, and a spatial scale of 64 pc/″.

Optically, the narrow line region (NLR) of NGC 4151 has been previously observed to be extended by about 4″ or 5″ along a position angle of 60°. Ulrich (1973) and Schulz (1990) spectroscopically identify a number of different velocity components or "clouds" at different distances within about 5″ of the nucleus along this position angle in [O III] and Hα emission. The NLR is resolved in narrowband [O III] images taken with the *Hubble Space Telescope* into a number of individual emission line clouds (Evans *et al.* 1993). These emission line clouds are themselves resolved on scales of less than 1″, and are distributed in northeast-southwest cones with opening angles of 75°±10°.

It is of interest to investigate how the spatial distribution of infrared line radiation in NGC 4151 compares to the spatial distribution of optical line radiation. Among the strongest near-infrared lines in Seyfert nuclei are the forbidden lines of singly ionized iron at $\lambda=1.2567$ μm and $\lambda=1.644$ μm. While the Fe$^+$ is excited by collisions with electrons and Fe$^+$ ions, the dominant physical processes responsible for the heating and ionization of the [Fe II] emitting gas in active galaxies are controversial, primarily due to the fact that iron is heavily depleted onto dust grains in the interstellar medium. In Seyfert galaxies, the central AGN, a circumnuclear starburst, or both could be responsible for the production of Fe+ and excitation of the [Fe II] emission (Mouri *et al.* 1993; Moorwood & Oliva 1988). Near-infrared [Fe II] emission is known to be strong in supernova remnants, and since starbursts are known to exist around some Seyferts such as NGC 7469 (Cutri *et al.* 1984, Wilson *et al.* 1986; Meixner *et al.* 1990; Mazzarella *et al.* 1994; Genzel *et al.* 1995), and NGC 1068 (Telesco & Harper 1980 Balick & Heckman 1985), the strong [Fe II] emission seen in some Seyferts may trace enhanced star formation.

Fast shocks and/or photoionization by hard x-rays from a source of high-energy ionizing radiation can be responsible

---

[1] Department of Astronomy and Astrophysics, 5640 S. Ellis, Chicago, IL 60637.

[2] Infrared Processing and Analysis Center, California Institute of Technology and Jet Propulsion Laboratory, MS 100-22, Pasadena, CA 91125.

0004-6256/96/112(1)/81/10/$6.00

for the creation of Fe^+ and the excitation of the near-infrared [Fe II] transitions in active galaxies. Shocks associated either with supernova remnants (SNR) in circumnuclear starbursts or with the interaction of radio jets with the extranuclear gas in Seyfert nuclei can effectively destroy dust grains thereby enhancing the gas phase iron abundance, and create partially ionized regions where much of the iron is in the form of Fe^+ (Forbes & Ward 1993). Alternatively, hard x-rays from a power-law ionizing source can create large partially ionized regions in which emission lines from low-ionization species such as O I, S II, N II, and Fe II are prominent. It is also possible that in some circumstances the Fe^+ abundance in such large partially ionized regions is high enough that it can account for all of the infrared [Fe II] emission, without the need for shocks to destroy grains (Mouri *et al.* 1993; Graham *et al.* 1990).

In this paper we present observations that address the origin of the near-infrared [Fe II] emission in NGC 4151. We report on spatially resolved spectroscopy of the near nuclear regions of NGC 4151, focusing on the [Fe II] $\lambda = 1.2567$ μm and Paβ $\lambda = 1.2818$ μm lines. We show that the width of the lines, their central velocities, and the [Fe II]/Paβ ratio vary with position along the slit; and that the [Fe II] emission is associated with previously identified clouds in the narrow-line region of NGC 4151.

2. OBSERVATIONS AND DATA REDUCTION

The observations described here were performed with the Hale 200 inch telescope at Palomar Observatory, using the new Palomar Near-Infrared Spectrometer (Larkin *et al.* 1995). On 1994 May 25, two spectra of 300 s each were obtained of NGC 4151 covering the spectral range between 1.24 and 1.30 μm. This spectral range includes Paβ (rest $\lambda = 1.2818$ μm) and [Fe II] (rest $\lambda = 1.2567$ μm). The spectra were obtained using a 0.75″ wide slit at a spectral resolution of $R \sim 1000$. The spatial scale of the camera on the spectrometer is 0.165″/pixel. The nucleus of the galaxy was moved back and forth along the slit by 20″ between observations, to allow for sky subtraction while continuously integrating on the object. The observations were made with the slit oriented at a position angle of 60°, to align it with the [O III] emission cones observed by the *Hubble Space Telescope* by Evans *et al.* (1993). Observing conditions were non-photometric. From observations of a point source and the spatial extent of the pointlike Seyfert 1 nucleus in the continuum, the full width at half maximum (FWHM) of the point spread function (PSF) was determined to be 1.3″. Immediately prior to the observations of NGC 4151, we observed the calibration star BS 4785 [G0 V]. A chopping secondary was used to uniformly spread the light of this star along the length of the slit. Spectral data frames were divided by the G-star spectral calibrator frames, in order to remove atmospheric absorption lines and to correct for efficiency variations across the field of view and gain variations across the array. The Paβ absorption feature in the G-star spectrum was removed before this division, in order to avoid the creation of artificial emission lines in the galaxy spectrum. Bad pixels in the array were removed by linear interpolation.

The spectral frames were corrected for large scale optical distortions in a two-step process. There is a small distortion due to the camera optics which leads to the curvature on the array of the spectrum of a point source. The continuum spectra of a point source (the G2 V star BS 8310), obtained at several locations along the length of the slit, were used to remove this distortion in the data. In addition, the fact that we are using a flat grating with an extended slit causes the spectrometer to image monochromatic light at the slit into a curved line at the focal plane of the spectrometer. The night sky OH emission lines of unsubtracted frames were used to measure and remove the curvature of the wavelength solution from the data frames. The two distortion corrected NGC 4151 spectra, spatially offset by 20″ along the slit, were subtracted from each other to remove sky emission, and the spectra were clipped to a $\sim 12''$ length along the spatial axis. The two clipped spectra were shifted so that their continua aligned, and were added together.

Despite the nonphotometric conditions of the observations, the spectra have been roughly flux calibrated using previous photometric J (1.25 μm) broadband observations (Neugebauer 1995) coupled with images obtained through the fully opened (10″ wide) slit at the time of the spectral observations. Photometry is performed through two synthetic beams on these images. One is a 7.5″ diameter beam set to match the beam of the photometric measurements, and the other is a rectangular beam with dimensions $1.0'' \times 0.75''$. The ratio of the signals observed in these two synthetic beams is equivalent to the ratio of the total amount of flux admitted through a 1.0″ length of the slit during the spectral observations to that of the previously measured flux of the galaxy. Under the assumption that the spectrum is approximately flat across the wavelength band in question, we can use this ratio together with the known spectral width of the J filter to flux calibrate the spectra. From the bright, point-like Seyfert 1 nucleus, we estimate that the seeing degraded by about 30% from the time of the imaging observations to the time of the spectral observations. Before performing the photometry in the $1'' \times 0.75''$ beam mentioned above, the images were convolved with a Gaussian profile to simulate this estimate of the seeing at the time of the spectral observations.

The largest source of systematic uncertainty in the flux calibration is the assumption that the continuum flux of the galaxy at the time of our observations was the same as it was at the time of the earlier photometric observations. The continuum of the nuclear source has been observed to fluctuate by as much as a factor of 2 at both 2.2 μm (Prestwich *et al.* 1992) and 0.5 μm (Antonucci & Cohen 1983). We therefore assume that our flux calibration is good to only 50%.

3. RESULTS

In Fig. 1 we present the two-dimensional near-infrared spectrum of NGC 4151. The vertical axis covers the 1.24–1.30 μm spectral regime, while the horizontal axis covers 7″ along the 0.75″ wide slit. Left corresponds to southwest (P.A. 240°), and right to northeast (P.A. 60°) on the sky. In Fig. 1b, a smoothed continuum and broad emission line of Pa β have been subtracted in order to increase the contrast

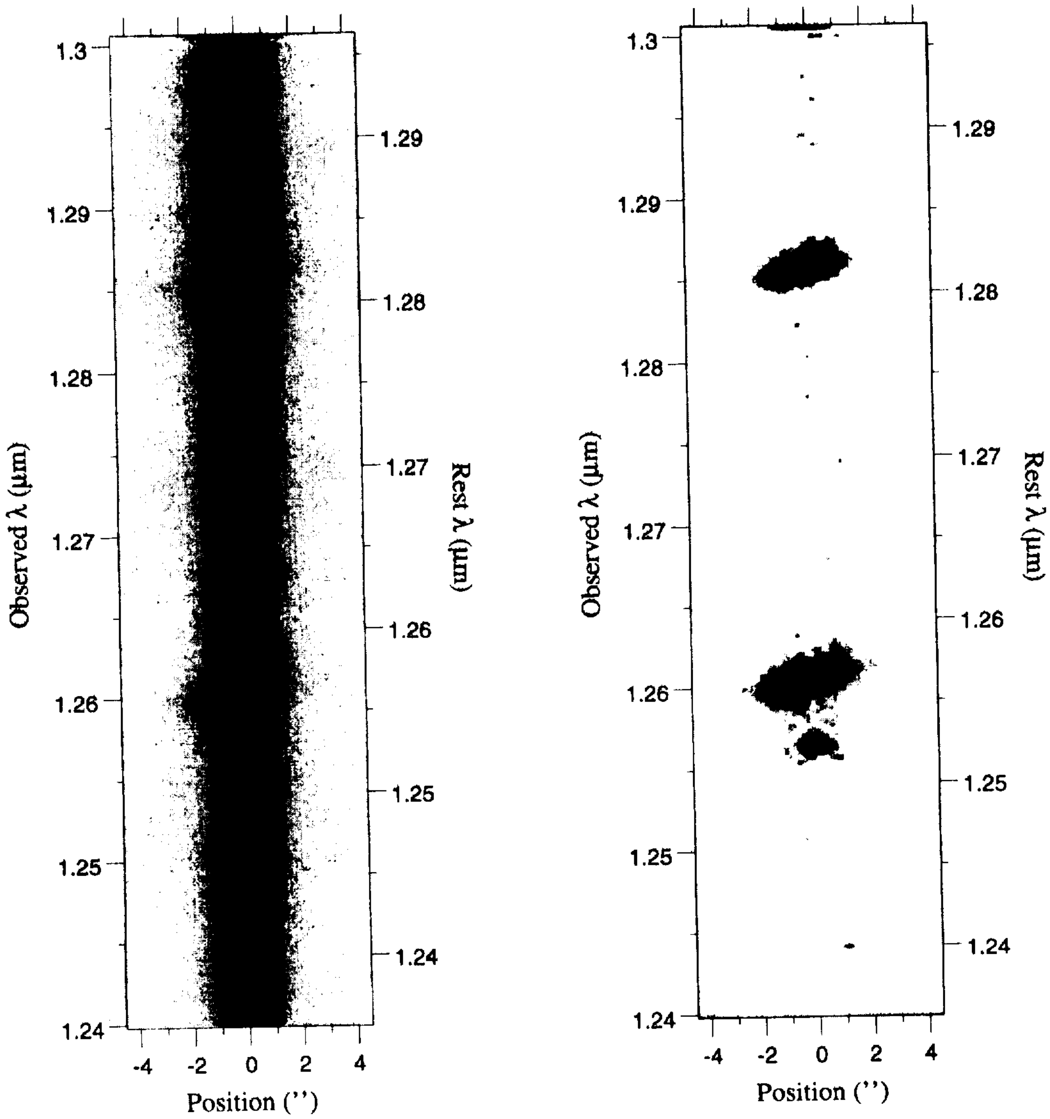

FIG. 1. A greyscale image showing the reduced 1.24–1.30 μm longslit spectrum of NGC 4151. The resolution of the spectrum is 240 km/s. On both spectra, the left axis scale is the observed wavelength, and the right axis is the rest wavelength, assuming a velocity of $cz=997$ km/s (Pedlar *et al.* 1992). The left image shows the full spectrum; the image on the right has a smoothed continuum and Paβ broad line subtracted, to increase the contrast of the narrow emission lines. In the left image, the contours are logarithmically scaled; in both images, the greyscale is linearly scaled. Three lines are visible on the plot: the upper line is Paβ (rest $\lambda=1.2818\mu$m), and below that is [Fe II] (rest $\lambda=1.2567$ μm). The line blueward of [Fe II] is [S IX] (rest $\lambda=1.25235$ μm).

and visibility of the narrow emission lines (see Appendix A). Three lines are visible in Fig. 1: Paβ ($\lambda=1.2818\mu$m), [Fe II] ($\lambda=1.2567$ μm), and a line at $\lambda=1.25235$ μm which we identify as [S IX]. This feature was first seen in the Circinus galaxy by Moorwood & Oliva (1994) and Oliva *et al.* (1994). Both the Paβ and [Fe II] lines are spatially extended, and show clear velocity shifts with position (visible as a tilt of the line on the figure). The [S IX] line is visible only on the nucleus, and is spatially unresolved, as distinct from the extended nature of the narrow components of Paβ and [Fe II]. This is consistent with the extent of coronal lines observed in the Circinus galaxy (Oliva *et al.* 1994), and in contrast with the prediction of Korista & Ferland (1989) that coronal lines would be extended at least as much as the narrow line region of an active galaxy. The [S IX] line does not show noticable velocity shifts; the single unresolved component on the nucleus is at a redshift of 973±46 km/s, consistent with the systemic velocity of the nucleus of NGC 4151. The line is not blueshifted with respect to the other lines on the nucleus, as is the case with other coronal lines in several Seyfert galaxies (Penston *et al.* 1984). Its FWHM, corrected for our instrumental resolution, is 170±65 km/s.

Figure 2 shows nine one-dimensional spectra, each extracted in 1.33" wide bins from the spectrum in Fig. 1. Each spatial bin is offset from adjacent ones by 0.67", one half of the width of a spatial bin. The 1.33" size of the spatial bin along the slit was chosen to match the seeing at the time of the spectral observations. The emission lines identified in Fig. 1 are clearly seen in Fig. 2. The Paβ line shows both broad and narrow components. On the nucleus there is a broad line with a FWHM of 5800± 800 km/s, and a total flux in a $1.33''\times0.75''$ beam of 800×10^{-15} erg cm^{-2} s^{-1}. The extent of the broad Paβ line is consistent with it being spatially unresolved.

The narrow component of Paβ is slightly resolved in velocity in some of the spatial bins: the spectral resolution is

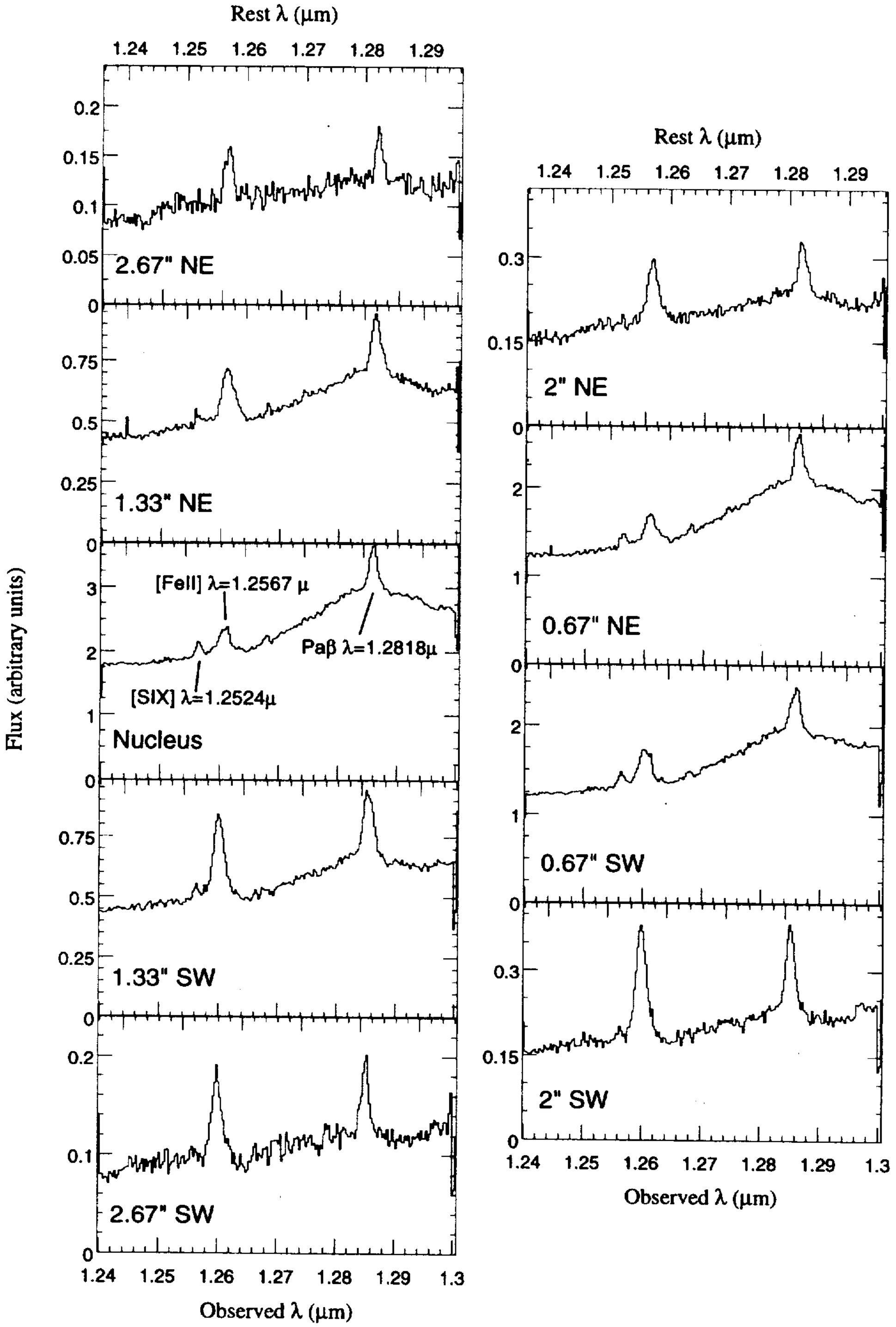

FIG. 2. One-dimensional infrared 1.24–1.30 μm spectra of the Seyfert 1.5 galaxy NGC 4151. These spectra show seven 1.33"×0.75" beams along a slit oriented at a position angle of 60°. The center spectrum on the left is for the nucleus, those above it northeast of the nucleus, those below it southwest of the nucleus. On the right are plotted spectra whose bins are offset spatially by one half the size of the spatial bin. Three strong lines are identified in the nuclear spectrum: the hydrogen recombination line Paβ, a forbidden line of ionized iron [Fe II], and a high-ionization forbidden line of sulfur, [S IX]. On the nucleus, a broad component of Paβ is also visible. This broad Paβ component is also visible in the bins adjacent to the nucleus as a result of its strength and the width of the psf (FWHM = 1.3"). From this figure, one can see that the centers of the narrow Paβ and [Fe II] lines, as well as the flux ratio of Paβ/[Fe II] vary along the length of the slit. The [S IX] line is only seen on the nucleus; its appearance in bins neighboring the nucleus is as a result of contamination due to our 1.3" psf.

240±20 km/s, based on unresolved atmospheric OH lines measured simultaneously with NGC 4151, while the typical intrinsic linewidth of Paβ is 250 km/s (after subtracting the width of an unresolved line in quadrature). The [Fe II] ($\lambda = 1.2567$ μm) line has no broad component. It also is clearly spatially resolved and appears broader than the narrow component Paβ, with a typical line width of 400 km/s after correction for our resolution.

TABLE 1. Line fluxes, velocities, and widths for the Paβ and [Fe II] emission lines observed in the spectrum of NGC 4151. The effective beam for each line is 1.33″×0.75″, so neighboring spatial bins overlap by 50%. The 0.75″ wide slit was oriented at a position angle of 60°. The uncertainties quoted on the fluxes include those in our flux calibration as well as those resulting from Gaussian fits described in the text of the paper (see text for detailed discussion). The instrumental resolution of 240 km/s, as measured from unresolved OH sky lines, has been subtracted in quadrature from the FWHM of each of the Gaussians in the table. For comparison, the systemic velocity of NGC 4151, as measured from the 21 cm H I line in outer parts of the galaxy, is 997±3 km/s (Pedlar *et al.* 1992).

	[Fe II] ($\lambda=1.2567$ μm)			Paβ ($\lambda=1.2818$ μm)		
Position	flux (10^{-15} erg s^{-1} cm^{-2})	center (km s^{-1})	FWHM (km s^{-1})	flux (10^{-15} erg s^{-1} cm^{-2})	center (km s^{-1})	FWHM (km s^{-1})
2.67″ NE	2.3±0.4	1033±31	260±50	2.3±0.4	1094±38	184±55
2.00″ NE	8.3±1.1	1056±28	490±21	5.5±0.8	1077±37	352±25
1.33″ NE	2.8±1.6	1389±129	405±160	1.8±1.0	1318±63	<180
	16.3±2.8	997±51	455±42	12.1±2.0	1001±39	280±39
0.67″ NE	5.3±3.5	1450±109	365±204	5.7±6.7	1253±204	336±298
	25.1±4.8	975±43	455±59	24.8±7.4	958±45	236±46
Nucleus	...	...	...	800	960±170	5800±800
	29.8±6.8	981±48	434±70	36.2±5.0	960±36	285±24
	6.9±6.0	487±148	402±342	...	...	...
0.67″ SW	37.2±5.1	855±28	575±20	16.9±6.8	1007±51	<180
	...	...	...	13.3±6.7	763±74	212±115
1.33″ SW	2.0±1.5	1318±167	455±332	5.3±3.0	1014±60	<180
	25.3±3.7	779±30	457±27	12.7±3.4	762±53	257±62
2.00″ SW	1.8±0.8	1245±71	335±148	...	...	...
	14.6±2.1	752±29	425±31	8.8±1.2	786±36	329±22
2.67″ SW	6.4±0.9	773±29	466±31	3.5±0.5	771±37	228±41

To determine the flux and shapes of the narrow lines, we first subtracted the continuum and broad Paβ line from the data to create a spectrum of the narrow lines above a zero continuum. We then fit one or more Gaussian line profiles to each narrow line in each of the nine 0.75″×1.33″ spatial beams spaced by 0.67″ in Fig. 2. Initially we fit a single Gaussian profile to each line (Paβ and [Fe II]) in each spatial bin, allowing the amplitude, width, and center of the Gaussian to vary in a χ^2 minimization fit. The fits were each performed individually and unconstrained; for example, the Gaussian profiles fit to the [Fe II] line were not required to have the same profile or velocity as those fit to the Paβ line at the same position on the slit. In many cases, this single Gaussian profile was sufficient to adequately fit the data. Where this provided a statistically unsatisfactory fit, an additional one or two Gaussian components were added. In all cases, we selected the minimum number of components to describe an individual feature. The simplest set of Gaussian profiles which adequately described the data for each line in each spatial bin is listed in Table 1. The fits are plotted with the data in Fig. 3. Appendix A discusses in greater detail those cases where more than one Gaussian line profile was required to fit the data. Although fitting the emission lines with Gaussian components does not provide a unique solution, it does allow for a simple means of describing the [Fe II] and Paβ line profiles as they change their shapes and centroids with distance from the nucleus.

4. DISCUSSION

4.1 *Identifying velocity components in Paβ*

The components of the Paβ line producing the observed shapes seen in Figs. 2 and 3 and in Table 1 are indicative of multiple, discrete emitting components rather than a continuous distribution of gas exhibiting a smooth velocity gradient. Were there a smooth distribution of gas, the line centers would vary smoothly in velocity with position away from the nuclear velocity. However, superimposed discrete components are visible, which change in relative strength causing the varying Paβ line profiles. A clear illustration of the nature of these multiple components is seen in the Paβ line southwest of the nucleus (Figs. 3n, 3o, 3p, and 3q). On the nucleus (Fig. 3n), the Paβ line is centered at 960 km/s. At a position 2.67″ southwest of the nucleus (Fig. 3q), the Paβ line is centered at 770 km/s. In the spatial bins 0.67″ and 1.33″ southwest of the nucleus (Figs. 3o and 3p), the Paβ emission can be described as an increasing mixture of the blueshifted 770 km/s component combined with the nuclear 960 km/s component. The nuclear component is stronger in the spatial bin 0.67″ southwest of the nucleus (Fig. 3o), with the blueshifted component visible as a blue shoulder. In the spatial bin 1.33″ southwest of the nucleus (Fig. 3p), the blueshifted component is stronger, with the nuclear component a red shoulder.

All of the velocity centers of the narrow Paβ Gaussian components tabulated in Table 1 are consistent with one of four basic velocity components: a nuclear component at about 980 km/s, consistent with NGC 4151's systemic velocity of 997 km/s (Pedlar *et al.* 1992), and consistent with the 960 km/s emission we observe on the nucleus, a blueshifted component southeast of the nucleus at about 770 km/s, a redshifted component visible >2″ northeast of the nucleus at about 1070 km/s, and a second redshifted component 1.33″ northeast of the nucleus at about 1380 km/s. From these identifications, a picture emerges of four cloud systems, at different velocities and distances from the nucleus, along the

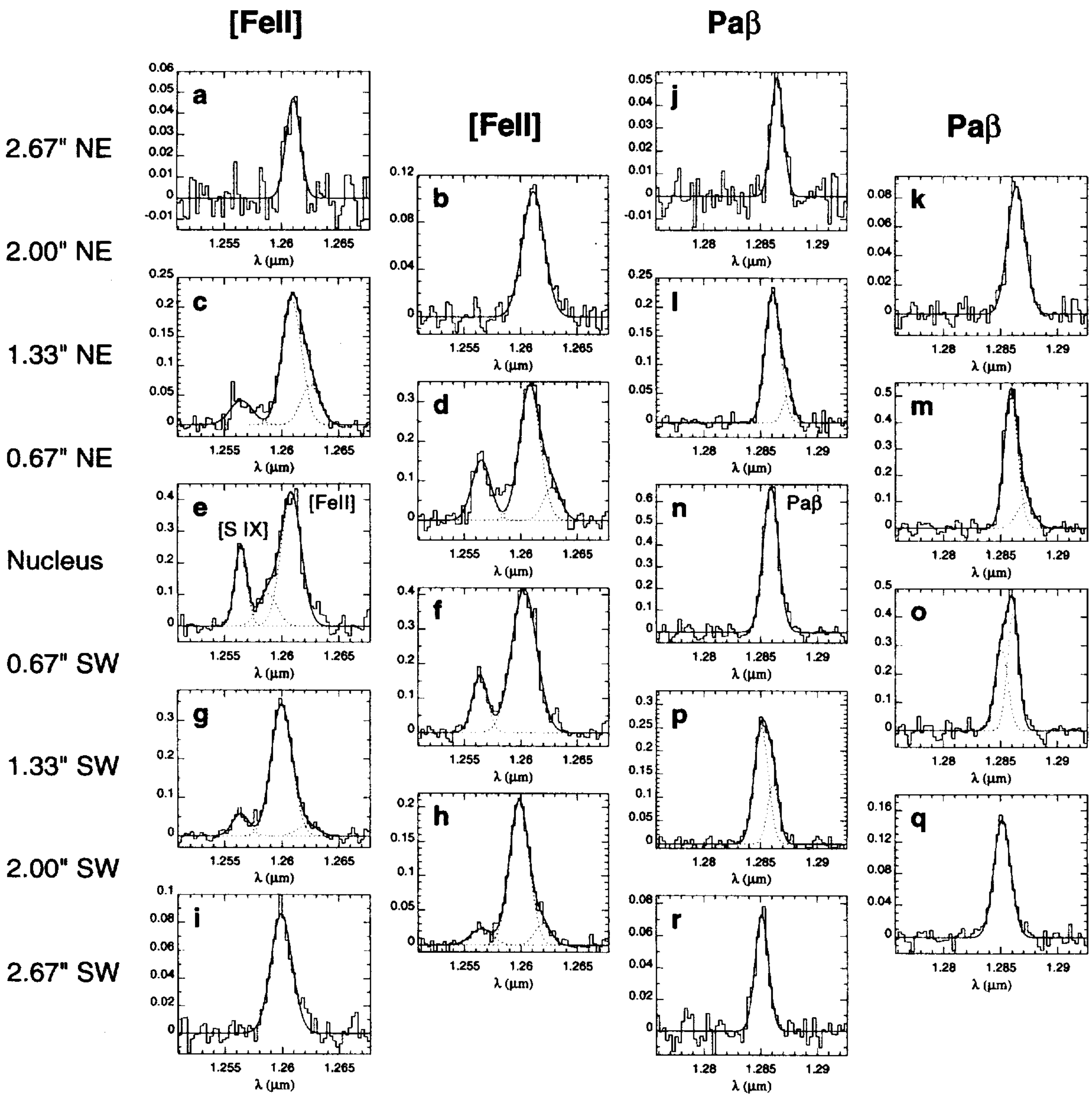

FIG. 3. Gaussian line profiles used to describe the [Fe II] and Paβ lines in each of the spatial bins of Fig. 2. Individual Gaussian line components are dotted lines, and the solid line is the sum of the individual Gaussian line profiles, indicating our total fit to the data. The narrow emission line on the blue side of [Fe II] seen in (c), (d), (e), (f), (g), and (h) is [S IX] (rest $\lambda = 1.25235$ μm). These fits are discussed in greater detail in Appendix A.

60° slit. A cartoon of this picture is shown in Fig. 4. Note that because the data in this paper are from a single slit orientation, we only have one dimension of spatial information.

Kinematically, the Paβ velocity components show correlations with the long slit optical Hα and [O III] spectroscopy of Schulz (1990) and Ulrich (1973). In the optical data, these authors identify a number of discrete components or "clouds" at velocities similar to the components seen here in the near-infrared lines. Table 2 lists the comparison between the kinematic components seen in the optical line and the kinematics seen in the near infrared lines in this paper. The optical data are used to model a nuclear outflow by Ulrich (1973) and Schulz (1990). There is remarkable agreement between the velocities of the optical and infrared emission lines suggesting that the latter are involved in the outflow from the Seyfert nucleus.

4.2 Correlation between Paβ and [Fe II]

The centroids of the components of the Paβ and [Fe II] lines as tabulated in Table 1 agree quite well with each other. Both are redshifted (relative to the nucleus) northeast of the nucleus, and both are blueshifted southwest of the nucleus. In general, the line shapes are similar within each spatial bin. For example, 1.33″ northeast of the nucleus, both the Paβ and [Fe II] lines have a red shoulder. In each spatial bin, with few exceptions there is good correspondence between the velocity centers of the two lines; usually, the components that comprise the [Fe II] line share the same redshifts as the

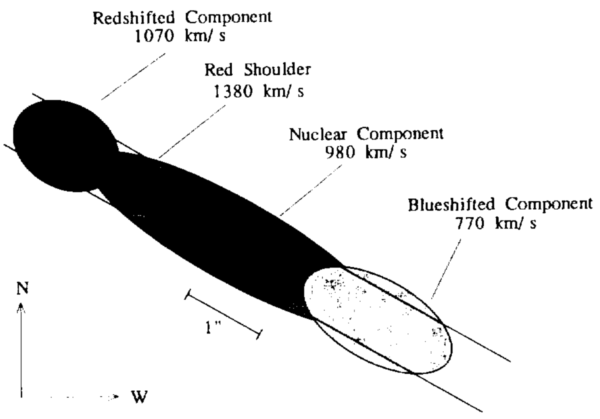

FIG. 4. A cartoon of the four narrow velocity components identified in Paβ and [Fe II] in Tables 1 and 2. The 0.75" wide slit at a position angle of 60° is indicated by the two long parallel lines. The cross indicates the center of the slit and the peak of the continuum emission.

components that comprise the Paβ line. One exception is 1.3" and 2.0" southwest of the nucleus, where there is a very weak red shoulder identified at approximately 1270 km/s in the [Fe II] line, which is not seen in Paβ. Given the ratios of [Fe II]/Paβ seen in the other components, it is possible this shoulder may just be too weak at Paβ to be identified in the spectra. A second exception to the correlation between line centers of Paβ and [Fe II] components is the [Fe II] emission 0.67" southwest of the nucleus (Fig. 3f), which, at a velocity centroid of 855±28 km/s, is intermediate between the nuclear system and the 770 km/s blueshifted system. Given the large width of this line (575±20 km/s) as compared to neighboring lines, this component is consistent with a blend of two Gaussian profiles, one at each of the velocities of these two systems. However, we cannot distinguish this blend from a single Gaussian fit. A final [Fe II] Gaussian component whose velocity center does not fall within one of the four velocity components identified in Paβ is the 487 km/s component identified on the nucleus (Fig. 3e). It is possible that this component is associated with the [S IX] line blueward of [Fe II] on the nucleus.

Except for the cases cited above, the Gaussian components fit to the [Fe II] lines belong to one of the four velocity systems identified in the Paβ line. Moreover, the [Fe II] emission components show the same velocity centers at the same locations along the slit as do the Paβ velocity components. The correlations between the Paβ and [Fe II] line velocities suggest that the cloud systems responsible for the narrow Paβ line are also producing the bulk of the [Fe II] emission. The correlations of the kinematics of the near infrared and optical lines further suggest that the [Fe II] emission arises in the narrow line region. Since the *HST* [O III] narrowband images of Evans *et al.* (1993) indicate structure on spatial scales an order of magnitude smaller than our spatial resolution, each velocity component we have identified is likely to be composed of many smaller clouds.

Although the line centroids of the [Fe II] and Paβ emission lines are generally well matched, the width of the [Fe II] line is consistently broader than that of the Paβ line in every spatial bin, and in every corresponding Gaussian component listed in Table 1. Given our spectral resolution of 240±20 km/s as measured from unresolved OH sky lines, most of the observed narrow Paβ features are unresolved or only marginally resolved in velocity, whereas the majority of the [Fe II] lines are clearly resolved in velocity, showing intrinsic widths of 400 km/s or more. The coincidence of the spatial and velocity centers of the Paβ and [Fe II] lines argue that the physical regions where each of these emission lines arise share the same large scale dynamics. The differences in the line widths, however, argue that on small scales there may be an additional excitation process acting upon the Fe$^+$.

Figure 5 is a plot of the line center versus the FWHM of the Gaussian components. On this figure are plotted all of the Gaussian profile fits from Table 1, excluding those points which because of their faintness and blending with adjacent components had an uncertainty in line width greater than 250 km/s and those points with an uncertainty in line centroid greater than 150 km/s. The blueshifted 770 km/s component, and the high velocity 1380 km/s component are easily

TABLE 2. Comparison of velocity components observed in this paper with velocity components observed in ground-based optical spectra (Ulrich 1973; Schulz 1990). For each velocity component, the table lists its distance from the nucleus along a position angle of 60°. The optical data listed are in both cases for [O III]; similar velocity structure is seen in Hα (Schulz 1990). The components reported for the J-band spectra presented here are seen in both Paβ and [Fe II] as discussed in the text.

	Ulrich (1973)		Schulz (1990)		this paper	
Component	position (at 240°)	velocity (km/s)	position (at 240°)	velocity (km/s)	position (at 240°)	velocity (km/s)
1	1.5" SW	(610)[a]	1-3" SW	740	1"-3" SW	770
2	nucleus	970	2"SW-2" NE	960	1.3" SW-1.3" NE	980
3	1"-3" NE	1120	2"-3" NE[b]	1130	2"-3" NE	1070
4	1" NE	(1470)[c]	...	...	1-2" NE	1380

Notes to TABLE 2

[a] This velocity is reported by Ulrich (1973) as the "blue edge" of the component.

[b] Schulz (1990) decomposes a flat-topped profile into two components, one at approximately the nuclear velocity of component 2 and the other at a velocity of 1130 km/s. Schulz (1990) identifies the 1130 km/s component with Ulrich's component having a red edge at 1470 km/s; here, that 1130 km/s component is instead identified with component 3 in the table.

[c] This velocity is reported by Ulrich (1973) as the "red edge" of the component.

TABLE 3. Variation of the narrow [Fe II]/Paβ flux ratio with position along the slit. The broad Paβ was not included in any of these flux ratios. The overall ratio of narrow [Fe II]/Paβ flux in our 0.75″×0.67″ slit is 1.28±0.04.

Position	[Fe II]/Paβ flux ratio
2.67″ NE	1.01±0.12
2.00″ NE	1.51±0.05
1.33″ NE	1.39±0.04
0.67″ NE	1.00±0.04
Nucleus	1.01±0.05
0.67″ SW	1.24±0.04
1.33″ SW	1.51±0.04
2.00″ SW	1.86±0.06
2.67″ SW	1.84±0.15

distinguished from each other and from the components closer to the nuclear velocity on this plot. The nuclear 980 km/s component and redshifted 1070 km/s component are not readily separated since their velocity difference is small and closer to the uncertainties in the various line centroids. The substantially larger [Fe II] line widths are immediately apparent in Fig. 5.

The infrared Paβ and [Fe II] emission is correlated, showing spatial and kinematic similarities which indicate the lines arise from the same or at least from correlated physical locations. Furthermore, the Paβ and [Fe II] emission shows similar velocity components to those seen in the optical NLR clouds. Consequently, our data argue that the [Fe II] emission arises in the NLR of NGC 4151, so there is no need to invoke a near-nuclear starburst to explain the [Fe II] emission.

4.3 [Fe II]/Paβ flux ratios and [Fe II] emission processes

The total narrow line flux ratio of [Fe II]/Paβ (excluding the broad Paβ line) in the 0.75″×6.67″ slit is 1.28±0.04. The ratio of [Fe II]/Paβ flux clearly varies as a function of position along the slit, and among the four previously mentioned velocity components. These results are summarized in Tables 3 and 4. The most noticeable trend evident in these tables is that the [Fe II]/Paβ ratio increases with increasing radius from the nucleus. This is true whether one considers just the ratio as a function of position (Table 3), or whether one considers the ratio for the four identified velocity components (Table 4, where the 980 km/s component is considered nuclear). The [Fe II]/Paβ flux ratios we observe are comparable to large-beam [Fe II]/Paβ flux ratios observed in other Seyfert galaxies, which typically range from 0.3 to 1.4 (Mouri *et al.* 1990; Goodrich *et al.* 1994).

TABLE 4. Variation of the narrow [Fe II]/Paβ flux ratio with velocity component. The four listed velocity components correspond to the four velocity components listed in Table 2. The 487 km/s component of [Fe II] on the nucleus (see Table 1) was not included in any of the flux ratios in the table. The [Fe II] 2.67″ northeast of the nucleus (at 1033±31 km/s) was considered to be part of the 1070 km/s velocity component. The [Fe II] emission at 855±28 km/s seen 0.67″ southwest of the nucleus was assumed to be an overlap of 50% the nuclear 980 km/s component and 50% the blueshifted 770 km/s component (see explanation in text and Fig. 5).

Component	[Fe II]/Paβ flux ratio
770 km/s	1.96±0.37
980 km/s	0.83±0.13
1070 km/s	1.84±0.15
1380 km/s	2.[illegible]3±2.34

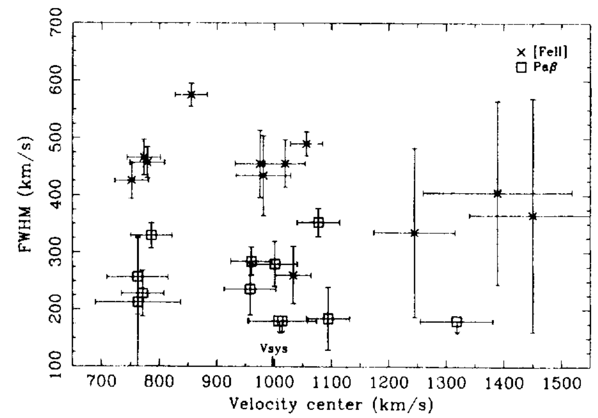

FIG. 5. Width vs central velocity of the Paβ and [Fe II] components tabulated in Table 1. Paβ is indicated by boxes and [Fe II] is indicated by crosses. For each of the three major velocity groupings, the [Fe II] line is broader than the Paβ lien by typically 150–200 km/s.

The large scale kinematical correlation between [Fe II] and Paβ observed is a direct indication that the [Fe II] emission arises in the NLR of NGC 4151. Additionally, the similarity between the near-infrared emission line components measured here and the optical Hβ and [O III] emission lines (Schulz 1990; Ulrich 1973) suggests the former arise in the outflowing ionized gas. However, the fact that the [Fe II] lines are consistently broader than the narrow Paβ lines argues for an additional excitation mechanism for the [Fe II]. This mechanism may be fast shocks associated with the outflow. These shocks could also explain the brightness of the [Fe II] emission, as shocks can destroy grains which contain much of the iron in the interstellar medium, thus increasing the gas phase abundance. If shocks do contribute to the [Fe II] emission, they ought to contribute to other low-ionization species as well. As such, one might expect other low-ionization species to show similar profiles to [Fe II] at the same spatial positions. Schulz (1990) tabulates the FWHM for several optical species, including [S II], [O I], and [N II]. For position angles close to 60° at a distance 2″ from the nucleus, the widths of these species are between 300 and 450 km/s, consistent with the linewidths observed for [Fe II]. However, the presence of multiple, possible overlapping emission line components in these data are difficult to assess. Multiple, marginally resolved components may be present; for example, in Hα southwest of the nucleus where the linewidth is >350 km/s (Schulz 1990), whereas in Paβ we separate two blended components each with width <250 km/s.

In the nearest Seyfert 2 galaxy, NGC 1068, Blietz *et al.* (1994) observe [Fe II] emission which is enhanced along the direction of the outflow from the nucleus. The strength of the [Fe II] emission drops where the radio jet flares out. Blietz *et al.* (1994) suggest that these features of the [Fe II] emission may be partially the product of shocks resulting from the interaction between the nuclear outflow and circumnuclear molecular clouds. Our correlation between [Fe II] and Paβ which indicates that the [Fe II] emission does arise in the NLR of NGC 4151, suggests that similar conditions may exist in the circumnuclear regions of both NGC 1068 and NGC 4151, and that similar processes may be giving rise to the [Fe II] emission.

Although shocks are a natural mechanism which can explain the enhanced [Fe II] emission in NGC 4151, we cannot rule out x-ray photoionization. From the flux ratio of [Fe II] (λ=1.644 μm)/Brγ in the Crab Nebula, Graham et al. (1990) argue that power-law photoionization of the filaments in the nebula produces enough partially ionized gas to account for all of the [Fe II] emission, and that there is no need for shocks to dissociate dust grains. From similarities between the [Fe II] to hydrogen recombination line flux ratios in the Crab Nebula and in NGC 4151 these authors further argue that photoionization in the NLR can entirely account for the [Fe II] emission in NGC 4151, with no need for shocks either from supernova or from the NLR itself. However, the fact that the [Fe II] line is systematically broader than the Paβ line in NGC 4151 suggests that another mechanism, possibly shocks, are important in the narrow line region for the generation of [Fe II] emission.

5. SUMMARY AND CONCLUSIONS

We have presented spatially resolved near-infrared spectroscopic data on the Seyfert 1.5 galaxy NGC 4151. There is a spatially unresolved broad component of Paβ a spatially unresolved component that we identify with [S IX] and spatially resolved narrow components of Paβ and [Fe II] (λ=1.2567 μm). From these data, we have identified individual velocity components in each of these lines, which have a finite number of discrete velocity centroids consistent with individual cloud systems, not with a smooth distribution of gas. The velocity centroids of the [Fe II] and Paβ lines agree well in spatial and velocity structure, indicating that these two species share similar bulk kinematics. In addition, the velocity components identified in our near-infrared data correspond well to velocity components previously identified in optical spectroscopy of NGC 4151. The correspondence in the kinematics of the [Fe II] line to the kinematics of the Paβ and optical Hβ and [O III] lines indicates that the [Fe II] emission is associated directly with the Seyfert narrow line region. Despite the strong correlation between the [Fe II] and Paβ velocity centroids, the [Fe II] narrow lines are consistently broader than the Paβ narrow lines. This suggests that the [Fe II] emission has an additional excitation source, possibly high velocity shocks associated with a nuclear outflow. The increase in the [Fe II]/Paβ line flux ratio with radius may reflect the increasing importance of this shock excitation to the [Fe II] with distance from the nucleus along the direction of the outflow.

The authors would like to thank Gerry Neugebauer for comments on this paper. We would also like to thank the night assistants at the 200″ telescope, Juan Carasco, John Moriarity, and James Hickey, as well as the rest of the staff of Palomar Observatory. Finally, we would like to thank the anonymous referee of this paper for helpful comments. Infrared astronomy at Caltech is supported by grants from NASA and the NSF.

APPENDIX: DISCUSSION OF INDIVIDUAL GAUSSIAN FITS

This Appendix discusses in greater detail the fits to the observed line profiles displayed in Figs. 2 and 3.

A.1 2.67″, 2.00″ Northeast of the Nucleus (Figs. 3a, 3b, 3j, 3k)

Both the [Fe II] line and the Paβ line were acceptably fit by a single Gaussian line profile in each of these spatial bins.

A.2 1.33″ Northeast of the Nucleus (Figs. 3c, 3l)

Both the Paβ and [Fe II] lines in this spatial have a non-Gaussian shape clearly visible in Fig. 2. Both lines appear to have a small "shoulder" on the long wavelength side. This red shoulder is also visible in the 0.67″ northeast bin in Fig. 2. Both lines were fit with two Gaussian line profiles. The fit was done by a χ^2 minimization of two profiles: one with a centroid near the peak in intensity of the entire line, and a second which fits the red shoulder. This procedure produces a significantly better fit (with a lower χ^2 per degree of freedom) to both line profiles than does a single Gaussian profile.

A.3 0.67″ Northeast of the Nucleus (Figs. 3d, 3m)

The [S IX] blueward of [Fe II] is present in this bin (Fig. 3d). It was fit with a single Gaussian profile. The [Fe II] line shows enhanced emission along its red shoulder. This was fit with a second, Gaussian profile redward of the primary [Fe II] component. In this spatial bin, the [Fe II] line was fit independently from the unidentified line.

The Paβ line (Fig. 3m), similar to the [Fe II] line, shows a small amount of enhanced emission on its red side. It also was fit with a second Gaussian profile redward of the primary Paβ component.

A.4 Nucleus (Figs. 3e, 3n)

Three Gaussian line profiles were required to adequately fit the [Fe II]/[S IX] line complex. The first is for the [S IX] line, which appears both in the nuclear spectrum, and the spectra 1.33″ northeast and southwest of the nucleus. The other two Gaussian profiles used to fit the profile of the [Fe II] line itself were centered on the peak of the emission, and a weaker "shoulder" necessary to fit the flux to the blue side of the peak. Figure 3e shows the results of this fit.

The broad Paβ line was fit to the unsubtracted spectrum of Fig. 2. One large source of uncertainty in the shape and the derivation of the integrated flux of the broad line is the shape of the continuum. To estimate the shape of the broad Paβ line and the uncertainties in the parameters that describe it, we used two different fits for the continuum: one, a flat and horizontal line (F_λ=const) at the level of the continuum at the left of the middle panel of Fig. 2, and two, a line sloping gently upward ($F_\lambda \propto \lambda$). Two Gaussians were simultaneously fit in a χ^2 minimization procedure over each of these continua, one to fit the broad line, one to model the narrow line. The results of these fits for the broad line are reported in Table 1. The results of these fits for the narrow line were consistent with the single Gaussian fit to the continuum and broad line subtracted spectrum.

A.5 0.67″ Southwest of the Nucleus (Figs. 3f, 3o)

One Gaussian profile for the [Fe II] line and one Gaussian profile for the [S IX] line was sufficient to fit the [FeII]/[S IX] complex (Fig. 3f).

The Paβ line (Fig. 3o) has an asymmetric shape, with a steeper drop redward of the peak than blueward of the peak. A good fit to the line included two Gaussian profiles of comparable amplitude.

A.6 1.33″ Southwest of the Nucleus (Figs. 3g, 3p)

Similar to the [Fe II] line 1.33″ northeast of the nucleus, this [Fe II] line appears to have a very weak red shoulder. A second Gaussian line profile was included in the χ^2 minimization fit to model this shoulder. In this case, the shoulder is at a velocity consistent with the redshift of the [Fe II] line on the nucleus, and the bulk of the [Fe II] emission is blueshifted relative to the nucleus.

The Paβ line (Fig. 3p) shows an asymmetry opposite that of the Paβ line 0.67″ southwest of the nucleus. As with the Paβ line 0.67″ southwest of the nucleus, it was fit with two Gaussian profiles of comparable amplitude.

A.7 2.00″ Southwest of the Nucleus (Figs. 3h, 3q)

One Gaussian profile was sufficient to fit the unidentified line blueward of [Fe II]. The [Fe II] line itself (Fig. 3h) shows enhanced emission in the red wing. It was fit with two Gaussian profiles: a strong one comprising the bulk of the line, and a weak second Gaussian profile redward of the center of the line to describe the enhanced wing emission.

The Paβ line (Fig. 3q) was satisfactorily fit with a single Gaussian profile.

A.8 2.67″ Southwest of the Nucleus (Figs. 3i, 3r)

The [Fe II] line and the Paβ lines were each adequately fit by a single Gaussian line profile.

REFERENCES

Antonucci, R. R. J., & Cohen, R. D. 1983, ApJ, 271, 564
Balick, B., & Heckman, T. 1985, AJ, 90, 197
Blietz, M., Cameron, M., Drapatz, S., Genzel, R., Krabbe, A., & Van Der Werf, P. 1994, ApJ, 421, 92
Cutri, R. M., Rudy, R. J., Rieke, G. H., Tokunaga, A. T., & Willner, S. P. 1984, AJ, 280, 521
Evans, I. N., Tsvetanov, Z., Kriss, G. A., Ford, H. C., Caganoff, S., & Koratkar, A. P. 1993, ApJ, 417, 82
Forbes, D. A., & Ward, M. J. 1993, ApJ, 416, 150
Genzel, R., Weitzel, L., Tacconi-Garman, L. E., Blietz, M., Cameron, M., Krabbe, A., & Lutz, D. 1995, ApJ, 44, 129
Goodrich, R. W., Veilleux, S., & Hill, G. J. 1994, ApJ, 422, 521
Graham, J. R., Wright, G. S., & Longmore, A. J. 1990, ApJ, 352, 172
Korista, K. T., & Ferland, G. J., 1989, ApJ, 343, 678
Larkin, J. E., Knop, R. A., Lin, S., Matthews, K., & Soifer, B. T. 1995, PASP (in press)
Mazzarella, J. M., Voit, G. M., Soifer, B. T., Matthews, K., Graham, J. R., Armus, L., & Shupe, D. 1994, AJ, 107, 1274
Meixner, M., Puchalsky, R., Blitz, L., Wright, M., & Heckman, T. 1990 ApJ, 354, 158
Moorwood, A. F. M., & Oliva, E. 1988, A&A, 203, 278
Moorwood, A. F. M., & Oliva, E. 1994, Infrared Phys. Technol., 35, 349
Mouri, H., Nishida, M., Taniguchi, Y., & Kawara, K. 1990, ApJ, 360, 55
Mouri, H., Kawara, K., & Taniguchi, Y. 1993, ApJ, 406, 52
Neugebauer, G. 1995, private communication
Oliva, E., Salvati, M., Moorwood, A. F. M., & Marconi, A. 1994, A&A, 288, 457
Osterbrock, D. E., & Koski, A. T. 1976, MNRAS, 176, 61P
Pedlar, A., Howley, P., Axon, D. J., Unger, S. W. 1992, MNRAS, 259, 369
Penston, M. V., Fosbury, R. A. E., Boskenberg, A., Ward, M. J., & Wilson, A. S. 1984, MNRAS, 208, 347
Prestwich, A. H., Wright, G. S., & Joseph, R. D. 1992, ApJS, 80, 205
Schulz, H. 1990, AJ, 99, 1442
Telesco, C. M., & Harper, D. A. 1980, ApJ, 235, 392
Ulrich, M. 1973, ApJ, 181, 51
Wilson, A. S., Baldwin, J. A., Sun, S. D., & Wright, A. E. 1986, ApJ, 310, 121